Monthly Notices
of the
ROYAL ASTRONOMICAL SOCIETY

MNRAS **471,** 4885–4893 (2017)
Advance Access publication 2017 August 9

doi:10.1093/mnras/stx1927

# Polarization properties of turbulent synchrotron bubbles: an approach based on Chandrasekhar–Kendall functions

N. Bucciantini[1,2,3]★

[1]*INAF – Osservatorio Astrofisico di Arcetri, Largo E. Fermi 5, I-50125 Firenze, Italy*
[2]*Dipartimento di Fisica e Astronomia, Università degli Studi di Firenze, Via G. Sansone 1, I-50019 Sesto F. no (Firenze), Italy*
[3]*INFN – Sezione di Firenze, Via G. Sansone 1, I-50019 Sesto F. no (Firenze), Italy*

Accepted 2017 July 21. Received 2017 July 21; in original form 2017 June 23

## ABSTRACT

Synchrotron emitting bubbles arise when the outflow from a compact relativistic engine, either a black hole or a neutron star, impacts the environment. The emission properties of synchrotron radiation are widely used to infer the dynamical properties of these bubbles, and from them the injection conditions of the engine. Radio polarization offers an important tool to investigate the level and spectrum of turbulence, the magnetic field configuration and possibly the degree of mixing. Here we introduce a formalism based on Chandrasekhar–Kendall functions that allows us to properly take into account the geometry of the bubble, going beyond standard analysis based on periodic Cartesian domains. We investigate how different turbulent spectra, magnetic helicity and particle distribution function impact on global properties that are easily accessible to observations, even at low resolution, and we provide fitting formulae to relate observed quantities to the underlying magnetic field structure.

**Key words:** polarization – radiation mechanisms: non-thermal – turbulence – ISM: bubbles – ISM: supernova remnants – radio continuum: ISM.

## 1 INTRODUCTION

Synchrotron emission originates from relativistic pairs spiraling in a magnetic field. In astrophysics synchrotron emission is a powerful tool to investigate relativistic plasmas and non-thermal particles distributions. These are the signatures of acceleration processes related often to relativistic engines, like neutron stars (as in the case of pulsars) and black holes [as in the case of active galactic nuclei (AGNs)].

One of the key properties of synchrotron emission is the high level of linear polarization (Westfold 1959; Legg & Westfold 1968), that theoretically can be as high as 70 per cent, for the typical particles distribution functions that are observed (quite often power laws). It was indeed thanks to its polarization that synchrotron emission was recognized for the first time in an astrophysical source, the Crab nebula (Baade 1956; Oort & Walraven 1956; Woltjer 1958a). When relativistic outflows interact with the surrounding environment, they tend to form synchrotron emitting bubbles. This happens for pulsars inside supernova remnants (Pacini & Salvati 1973; Rees & Gunn 1974; Kennel & Coroniti 1984; Gaensler & Slane 2006; Bucciantini 2008) leading to pulsar wind nebulae (often referred as *plerions*) that are characterized by a broad-band emission ranging from radio to X-ray (and TeV due to Inverse Compton). It also happens for Radio lobes fed by the jet produced in AGNs (Scheuer 1982; Begelman, Blandford & Rees 1984; Begelman & Cioffi 1989; Carilli, Perley & Harris 1994; Reich, Testori & Reich 2001). The study of radio emission and polarization enables us to infer information on the strength and structure of the magnetic field that are relevant to understand the dynamics of these systems. For example, in pulsar wind nebulae, radio emission traces old particles that fill the entire volume of the nebula and it is detectable also in old systems, where the injection from the pulsar has faded away (Frail et al. 1996; Giacani et al. 1997; Roberts et al. 1999; Ma et al. 2016). Recent observations (e.g. Ma et al. 2016) and a set of theoretical indications based either on numerical simulations (Jun 1998; Blondin, Chevalier & Frierson 2001; Porth, Komissarov & Keppens 2014) or on spectral modelling (Tang & Chevalier 2012; Olmi et al. 2015, 2016; Tanaka & Asano 2016) suggest that a non-negligible level of turbulence should be present in these systems. Some simplified model for the turbulent field has already been presented attempting to explain some of the observed results (Ma et al. 2016; Bucciantini et al. 2017). The level of turbulence in wind bubbles could be important to understand how particles diffuse (Tang & Chevalier 2012), the level of mixing and penetration of the ambient medium (Blondin et al. 2001), the strength of the magnetic field (its ability to quench the cascade) and its role in the nebular dynamics (Bucciantini et al. 2004).

There is vast literature that in the past years has focused on modelling the polarized properties of synchrotron emission, in a

★ E-mail: niccolo@arcetri.astro.it

turbulent magnetic field, but most of it has focused on the Galactic background emission associated with cosmic rays (e.g. Lazaryan & Shutenkov 1990; Lazaryan & Chibisov 1991; Waelkens, Schekochihin & Enßlin 2009; Junklewitz & Enßlin 2011; Lazarian & Pogosyan 2012a, 2016). Far less has been done in the case of confined systems, like wind bubbles. Part of the problem is due to the fact that the techniques developed for the former are of little use in the latter. In general the approaches to modelling the polarized properties of synchrotron emission, in a turbulent magnetic field, are based on the idea of an infinitely extending volume, where the turbulence is homogenous (Thiébaut et al. 2010; Lazarian & Pogosyan 2012b; Herron et al. 2016; Zhang et al. 2016) and make use of internal Faraday rotation, which is not present for a pair plasma (as expected in pulsar wind nebulae). Assuming homogeneous, infinitely extending turbulence, is equivalent to neglecting any physical scale of the system under investigation (they are all much larger than any of the scale of the turbulent cascade). Unfortunately this is not the case for wind bubbles, where the scales of the turbulent cascade are comparable with the bubble dimension itself. On top of this we need to recall that several mathematical tools have been developed through the years to deal with turbulence in a homogenous infinite space, while the case of a confined volume (where surface effects are important), being more dependent on the specific boundary conditions, has been hardly touched. Finally, numerical tools exist that are efficient, and easy to implement to work in Cartesian domains with periodic boundaries (think the fast Fourier transform) that are not available on other domains or for other geometries.

In this work we present a new approach to the study of turbulent magnetic field configurations inside confined domains, and in particular we select a spherical domain, which can be thought of as a good first-order approximation for an emitting bubble, based on an alternative set of harmonic functions with respect to Fourier plane waves. Our approach is based on Chandrasekhar–Kendall functions (CK; Chandrasekhar & Kendall 1957; Chandra 1987). CK functions have been used for modelling spheromak configurations (Vandas et al. 1997; Dasgupta et al. 2002), plasmoid in the solar corona (Burlaga 1988; Chandra & Prasad 1991; Farrugia, Osherovich & Burlaga 1995; Vandas, Fischer & Geranios 1991) and for dynamos in confined domains (Mininni & Montgomery 2006; Mininni, Montgomery & Turner 2007; Brandenburg 2011). They are the natural extension of Fourier modes to spherical geometry, but they can be extended also to other geometry (Rasband & Turner 1981) as in the case of shells (Morse 2007), cylinders (Marsh 1992; Morse 2005) or ellipsoids (Ivanov & Kharshiladze 1985). They allow us to set the proper boundary conditions for a confined field and to take into account the geometry of the emitting region in a formally correct way (instead of truncating the emission at the edge of a given volume without care of the magnetic field structure). This allows us to take into account volumetric effects. Given that the scope of this paper is to characterize the signature of a turbulent field, providing estimates that could easily help guide the interpretation of observations, we focus our attention on global quantities that are easily measurable even at the typical low resolution, at which synchrotron bubbles are observed.

In Section 2, we introduce the formalism that we adopt to model a turbulent magnetic field confined within an emitting bubble. In Section 3 we derive some simple scaling of quantities that will be analysed in Section 4 where we present the result of a statistical study of the global polarized properties for synchrotron emitting bubbles. In Section 5 we present our conclusions.

## 2 MAGNETIC FIELD REALIZATION

We are going to discuss here how to implement a magnetic field realization on a spherical domain, such that we can enforce the specific boundary condition of full confinement at the spherical surface bounding the domain itself, in a rigorous manner. The idea is to use spherically adapted harmonic function instead of simple Cartesian Fourier modes. Note that the use of adapted harmonic functions can be extended to a variety of different geometries, for which they are defined.

### 2.1 Chandrasekar–Kendall functions

In spherical coordinates $[r, \theta, \phi]$, given the scalar function:

$$\Upsilon_{nlm} = J_l(k_{nl} r) Y_l^m(\theta, \phi), \tag{1}$$

where $J_l$ is the spherical Bessel function of the first kind of degree $l$, $Y_l^m$ is the real spherical harmonic of degree $l$, $m$ and $k_{nl}$ is the $n$-th zero of $J_l$, the vector field defined by

$$\boldsymbol{B}_{\pm nlm} = \pm k_{nl} \nabla \wedge [\Upsilon_{nlm} \boldsymbol{r}] + \nabla \wedge \nabla \wedge [\Upsilon_{nlm} \boldsymbol{r}] \tag{2}$$

is a force free field $\pm k_{nl} \boldsymbol{B}_{\pm nlm} = \nabla \wedge \boldsymbol{B}_{\pm nlm}$ with vanishing radial component of the unitary 2-sphere $\mathcal{S}$: $\boldsymbol{B}_{\pm nlm} \cdot \boldsymbol{e}_r = 0$ at $r = 1$. Being force free (Woltjer 1958b; Molodensky 1974), this vector field is also solenoidal and it is known as *Chandrasekhar –Kendall* functions. It can be shown that CK functions form a complete basis for solenoidal vector fields in the unitary ball $\mathcal{B}$, with vanishing component on the boundary $\mathcal{S}$ [Yoshida (1992); Mininni & Montgomery (2006); Mininni et al. (2007), see for example Deredtsov, Kasantsev & Schuster (2007) for other basis]. CK functions can be written in terms of real vector spherical harmonics:

$$\begin{aligned}\boldsymbol{B}_{\pm nlm} = & \frac{l(l+1)}{r} J_l(k_{ln} r) \boldsymbol{Y}_l^m + \left[ \frac{\mathrm{d}}{\mathrm{d}r} J_l(k_{ln} r) + \frac{J_l(k_{ln} r)}{r} \right] \boldsymbol{\Psi}_l^m \\ & + \pm k_{ln} J_l(k_{ln} r) \boldsymbol{\Phi}_l^m, \end{aligned} \tag{3}$$

where $\boldsymbol{Y}_l^m = Y_l^m \boldsymbol{e}_r$, $\boldsymbol{\Psi}_l^m = r \nabla Y_l^m$ and $\boldsymbol{\Phi}_l^m = r \boldsymbol{e}_r \wedge \nabla Y_l^m$. CK functions are, moreover, orthogonal in the sense that

$$\int_{\mathcal{B}} \boldsymbol{B}_{anlm} \cdot \boldsymbol{B}_{efgh} \mathrm{d}^3 x = l(l+1) J_{l+1}^2(k_{nl}) k_{nl}^2 \delta_n^f \delta_l^g \delta_m^h \delta_a^e \tag{4}$$

where $a, e = \pm$ and $\delta_a^e = 1$ only if $a$ and $e$ are the same sign.

### 2.2 Magnetic field, power spectrum and CK functions

Given the properties of CK functions any magnetic field bound to be confined into a spherical region of unitary radius can be written as the sum of CK modes

$$\boldsymbol{B} = \sum_{\pm} \sum_{n=1}^{\infty} \sum_{l=1}^{\infty} \sum_{m=-l}^{l} c_{\pm nlm} \boldsymbol{B}_{\pm nlm}, \tag{5}$$

where the first sum is done on CK functions of a different sign. Being the modes orthogonal, for the magnetic field defined in equation (5), it is possible to write the total energy $E$, the total helicity $H$, the total current helicity $I$ in $\mathcal{B}$ as

$$E = \sum_{\pm} \sum_{n=1}^{\infty} \sum_{l=1}^{\infty} \sum_{m=-l}^{l} c_{\pm nlm}^2 l(l+1) J_{l+1}^2(k_{nl}) k_{nl}^2 \tag{6}$$

$$H = \sum_{\pm} \sum_{n=1}^{\infty} \sum_{l=1}^{\infty} \sum_{m=-l}^{l} \pm c_{\pm nlm}^2 l(l+1) J_{l+1}^2(k_{nl}) k_{nl} \tag{7}$$

$$I = \sum_{\pm} \sum_{n=1}^{\infty} \sum_{l=1}^{\infty} \sum_{m=-l}^{l} \mp c^2_{\pm nlm} l(l+1) J^2_{l+1}(k_{nl}) k^3_{nl} \tag{8}$$

Note that modes with the same $n$, $l$ but different $m$ are degenerate in energy. It is immediately obvious that the decomposition in CK functions allows one to control the helicity of the field and to build magnetic field configurations having the same total energy but with various possible prescription for the helicity:

(i) *maximal helicity realization* if $c_{-nlm} = 0$ (or equivalently $c_{+nlm} = 0$) for all $n$, $l$, $m$. In this case all CK modes contribute an helicity of the same sign and the total helicity is maximal;
(ii) *zero helicity realization* if $c_{-nlm} = c_{+nlm}$ for all $n$, $l$, $m$. In this case the same power goes into CK modes of opposite helicity and the total helicity vanishes;
(iii) *definite helicity realization* if $c_{-nlm} = 0 \Leftrightarrow c_{+nlm} \neq 0$ for all $n$, $l$, $m$. In this case all the power for each CK mode goes into a definite helicity state, even if the sign differs for different modes; and
(iv) *random helicity realization* if no constraints are imposed on $c_{\pm nlm}$ for all $n$, $l$, $m$. In this case the power for each CK mode is randomly distributed in the two possible helicity states.

In general, when using Fourier decomposition in finite Cartesian domains, turbulent magnetic field realizations are built assigning at each mode of wavenumber $\boldsymbol{k}$ an amplitude such that when integrating the energy contribution in the volume of all modes up to any arbitrary value of the wavenumber norm $k_{\rm max}$ one finds

$$E(k_{\rm max}) = \sum_{\boldsymbol{k}}^{1<k<k_{\rm max}} E(\boldsymbol{k}) = \int_1^{k_{\rm max}} P(k) {\rm d}k, \tag{9}$$

where $E(\boldsymbol{k})$ is the energy associated with the Fourier mode of wavenumber $\boldsymbol{k}$ and $P(k)$ is the on-shell power spectrum (representing all the energy at a wavenumber $k$), and $k = 1$ is the first allowed mode. Usually Fourier modes are quantized, given that in a finite domain only modes that are periodic are allowed. Fourier decomposition is however just a special case of decomposition into harmonic functions, corresponding to plane waves, adapted to a Cartesian domain. In different geometries other harmonic decompositions might prove more suitable (one can for example define properly the boundary conditions on a spherical shell). In spherical geometry, one can use for example spherical waves defined in term of Bessel functions and spherical harmonics as equation (1). It can be shown that it is always possible to transform from one to the other (Mininni & Montgomery 2006; Mininni et al. 2007; Liao & Su 2015). CK function can be seen as a generalization to spherical geometry of Fourier modes. In particular given that each CK mode has maximal helicity, they are the spherical equivalent of Beltrami waves. Boundary conditions set the quantization of the modes $[J_l(k_{nl}) = 0]$.

If $P(k) \propto k^{-\delta}$, with $\delta > 1$ then

$$\sum_{\pm} \sum_{n,l=1}^{k_{nl}<k_{\rm max}} \sum_{m=-l}^{l} c^2_{\pm nlm} l(l+1) J^2_{l+1}(k_{nl}) k^2_{nl} \propto k^{1-\delta}_{\rm max}. \tag{10}$$

This condition translates into a condition on the coefficients of the realization:

$$\sum_{\pm} \sum_{m=-l}^{l} c^2_{\pm nlm} = \frac{1}{l(l+1)} \frac{k^{-\delta-1}_{nl}}{J^2_{l+1}(k_{nl})}. \tag{11}$$

How this power is distributed amongst modes of different sign, depends on the helicity prescription. On the other hand the distribution amongst the various $m$ depends on the isotropy of turbulence. It is well known that MHD turbulence is anisotropic (Goldreich & Sridhar 1995; Brandenburg & Lazarian 2013), with the anisotropy dependent on scale. For simplicity, in our realizations we assume isotropy. For a solenoidal magnetic field, isotropy implies that all directions are equally probable for the orientation of each multipole of degree $nl$. Given the known rotational properties of spherical harmonics, in each realization we achieve this by randomly distributing the power of the multipole amongst the various $m = -l, ..., 0, ..., l$ subject to the normalization given by equation 11. In practice for each value of $n$ and $l$ we generate $2(2l + 1)$ random number in the interval $[-1, 1]$, (where the factor 2 comes from the presence of modes with two signs: the $\pm$ part), we set each of the $c_{\pm nlm}$ equal to one of these random numbers, and then we renormalize them such that the sum of their squared over $\pm$ and $m = -l, l$ satisfies the condition of equation (11). This ensures that 1: on a single realization, the spatial orientation of the various multipoles $nl$, are uncorrelated; and 2: that averaged over many realizations, the orientation of each of the various multipoles, over which the field is decomposed, is uniform on the 2-sphere. So, for us 'isotropy' means that in each realization the various multipoles are randomly oriented and there is no preferential alignment amongst them. Please note that the uniform assumption holds for the ensemble of realizations.

### 2.3 Numerical setup and simulated synchrotron maps

Turbulent magnetic field realizations are built on a 3D Cartesian grid containing the unitary sphere. The resolution has been chosen such that the results on the quantities of interest are converged. Assuming a power law distribution of emitting pairs:

$$n(\epsilon) = K \epsilon^{-(2\alpha+1)}, \tag{12}$$

where $\epsilon$ is the energy in units $m_e c^2$ and $K$ in principle could be a function of position. The emissivity towards the observer (assumed to be located along the $x$-axis) at a frequency $\nu$ is

$$j(\nu) = C \mid \boldsymbol{B} \times \boldsymbol{n} \mid^{\alpha+1} \nu^{-\alpha} \tag{13}$$

where $\boldsymbol{n} = \boldsymbol{e}_x$ and $C$ is given by synchrotron theory

$$C = \frac{\sqrt{3}}{4} \frac{\alpha + 5/3}{\alpha + 1} \Gamma\left(\frac{\alpha + 5/3}{2}\right) \Gamma\left(\frac{\alpha + 1/3}{2}\right) \times \frac{e^3}{mc^2} \left(\frac{3e}{2\pi mc}\right)^{\alpha} K. \tag{14}$$

Assuming the $y$ and $z$ coordinates to lay on the plane of the sky, it is possible to compute the maps of the various Stokes parameters integrating the contribution of each fluid element along the line of sight through the domain of the realization, according to

$$I(\nu, y, z) = \int_{-\infty}^{\infty} j(\nu, x, y, z)\, {\rm d}x, \tag{15}$$

$$Q(\nu, y, z) = \frac{\alpha + 1}{\alpha + 5/3} \int_{-\infty}^{\infty} j(\nu, x, y, z) \cos 2\chi \, {\rm d}x, \tag{16}$$

$$U(\nu, y, z) = \frac{\alpha + 1}{\alpha + 5/3} \int_{-\infty}^{\infty} j(\nu, x, y, z) \sin 2\chi \, {\rm d}x, \tag{17}$$

where the local polarization position angle $\chi$ is the angle of the emitted electric field vector in the plane of the sky, such that

$$\cos 2\chi = \frac{B_y^2 - B_z^2}{B_y^2 + B_z^2}, \qquad \sin 2\chi = -\frac{2 B_y B_z}{B_y^2 + B_z^2}. \tag{18}$$

The total intensity $I$ and total polarized intensity $I_{\rm p} = \sqrt{U^2 + Q^2}$, can be obtained integrating the various Stokes parameters over the $(y, z)$ −plane of the sky.

## 3 CASCADE ENERGY AND TOTAL BRIGHTNESS

If the turbulent cascade extends up to a maximum value $k_{\rm max}$ one can model the total emission from the unitary sphere of volume $V$ as the sum of the emission coming from $n \approx V k_{\rm max}^3$ regions inside which the magnetic field can be taken as uniform. For a random Gaussian realization, in each of these regions, the field orientation and strength will be randomly distributed. If the emitting particles are uniformly distributed, then the total intensity $I$, integrated over the emitting area, will just be function of the magnetic field:

$$I \propto \sum_n (B \sin\theta)^{\alpha+1} = n\langle (B\sin\theta)^{\alpha+1}\rangle = n\langle B^{\alpha+1}\rangle\langle(\sin\theta)^{\alpha+1}\rangle, \tag{19}$$

where $\theta$ is the angle between the magnetic field $\boldsymbol{B}$ and the direction of the observer $\boldsymbol{n}$, we have used the definition of mean and the fact that direction and strength of the magnetic field are uncorrelated variables, for isotropic turbulence. For any quantity $Q$ having a Maxwellian distribution (like the strength of the magnetic field), it can be shown that $\langle Q^\alpha\rangle \propto$ lang;$Q\rangle^\alpha$, hence we find:

$$I \propto \langle B^2\rangle^{(\alpha+1)/2} \propto E^{(\alpha+1)/2}. \tag{20}$$

Then one can estimate how the total brightness depends on $k_{\rm max}$:

$$I(k_{\rm max}) \propto E(k_{\rm max})^{(\alpha+1)/2} = [E(k_\infty) - \delta E(k_{\rm max})]^{(\alpha+1)/2}, \tag{21}$$

$$I(k_{\rm max}) = I(\infty)[1 - \delta E(k_{\rm max})/E(\infty)]^{(\alpha+1)/2}, \tag{22}$$

where $E(\infty)$ and $I(\infty)$ are the magnetic energy and total intensity of a realization extending to $k = \infty$, respectively, and we have introduced the quantity $\delta E(k_{\rm max})$, which represents the difference of the magnetic energy between a turbulent cascade extending to $k = \infty$ and one up to $k_{\rm max}$. For the polarized intensity $I_{\rm p} = \sqrt{U^2 + Q^2}$ instead, one must recall that unlike $I$, $Q$ and $U$ are not positively defined. For a realization extending up to $k_{\rm max}$, there will be $\approx k_{\rm max}^3$, domains that contribute to the polarized intensity incoherently. So we expect that the contribution to the polarized intensity from these domains should scale as the variance of the total intensity. The difference in polarized intensity between a turbulent cascade extending to $k = \infty$ and one up to $k_{\rm max}$.

$$\delta I_{\rm p}(k_{\rm max}) \propto \delta E(k_{\rm max})^{(\alpha+1)/2} k_{\rm max}^{-3/2} \propto \delta E(k_{\rm max})^{(\alpha+1)/2+3/2(\delta-1)} \tag{23}$$

suggesting that for typical values of $\delta$ and $\alpha$, the polarized intensity should typically saturate within few per cent already at $\delta E(k_{\rm max}) \sim 0.2$.

## 4 RESULTS

We have computed models for various values of the turbulent spectral index, $\delta = [4/3,\ 3/2,\ 5/3,\ 11/6,\ 2]$, and particle distribution function $\alpha = [0,\ 1/4,\ 1/2]$. The turbulent index has been chosen in order to include both Kolmogorov $\delta = 5/3$ and Kraichnan $\delta = 3/2$ scaling. The particle distribution function has been chosen to target the typical radio spectrum of Pulsar Wind Nebulae (PWNe) (for the Crab nebula $\alpha = 1/4$). For each value of $\delta$ and $\alpha$ we computed synchrotron maps for one hundred different random realizations, for which the uniform assumptions holds as an ensemble, which allowed us to compute the ensemble mean values of observable quantities and to estimate their typical variances $\sigma$. In order to get converged results on the quantities of interest, we found that each realization must include at least $10^4$ CK modes (this means that we have to compute at least $10^4$ coefficients $c_{\pm nlm}$ and the related Bessel functions and spherical harmonics). Taking the turbulent spectrum to be a pure power law corresponds to the assumption that the coherence scale of the turbulence is the size of the bubble itself. We focus our attention to global quantities that are easily accessible to simple measures. Quantities like the two-points correlation function or the Fourier spectrum of the emission map, while far more informative, in general require the object to be observed at a very high resolution, which is often not the case for our typical targets (PWNe).

### 4.1 Maximal helicity

We present here the results in the simplest case where the emitting particles (pairs) are distributed uniformly in space ($K$ is constant in space), and the magnetic field follows a realization with maximal helicity: $c_{-nlm} = 0$. In Fig. 1 we compare brightness maps in polarized intensity obtained from realizations with different turbulent power spectra, but where the power at each $k$ is distributed in the same proportion amongst the degenerate modes (the relative orientation of the modes is the same), such that the final maps have the same structure. As expected, realizations with smaller values of $\delta$ tend to show more fine structures, however the difference is quite small, and it would require a very high resolution and high signal-to-noise observations to be detected. On the contrary we found that the polarized intensity, once normalized to the average unpolarized brightness is quite sensitive to the value of $\delta$. Another feature that is commonly found in our realizations is the presence of one or two highly polarized spots, where the typical polarized intensity is about twice the average nebular value, and which in general are not coincident with the brightest regions in the total intensity. As shown in the figure, these highly polarized spots are not necessarily located close to the centre, first because synchrotron emissivity strongly depends on the orientation of the magnetic field, and in general there is no reason for the magnetic field to be preferentially orthogonal to the line of sight close to the centre of the bubble. Secondly being maps in polarized intensity, one should remember that there are depolarization effects once one integrates along the line of sight over regions with different magnetic orientations. So polarized emission will peak where, by chance of the realization, these depolarization effects are minimal, and these regions might or might not be close to the centre. On the other hand the polarized fraction tends to rise at the very edges of the bubble where it can reach values close to the theoretical maximum $(\alpha + 1)/(\alpha + 5/3)$, in the body of the emitting bubble one finds either unpolarized regions and regions with polarization as high as 50 per cent of the theoretical maximum. Please note that the maps shown correspond just to one realization, in order to provide an idea of the results to the reader, but are not meant to represent any typical average. They are mean to illustrate how a different choice of the turbulent index $\delta$, quenching or instrumental resolution affects the appearance of a map in polarized intensity.

In Fig. 2 we show the mean (ensemble averaged over many realizations) of the polarized fraction defined as the ratio of total polarized intensity over total intensity: $PF = I_{\rm p}/I$ with error-bars indicating the $2\sigma$ range of the results computed over a hundred different realizations. The $\delta = 1$ point is set at $PF = 0$, according to the discussion of Section 3, because for $\delta = 1$ the total intensity is

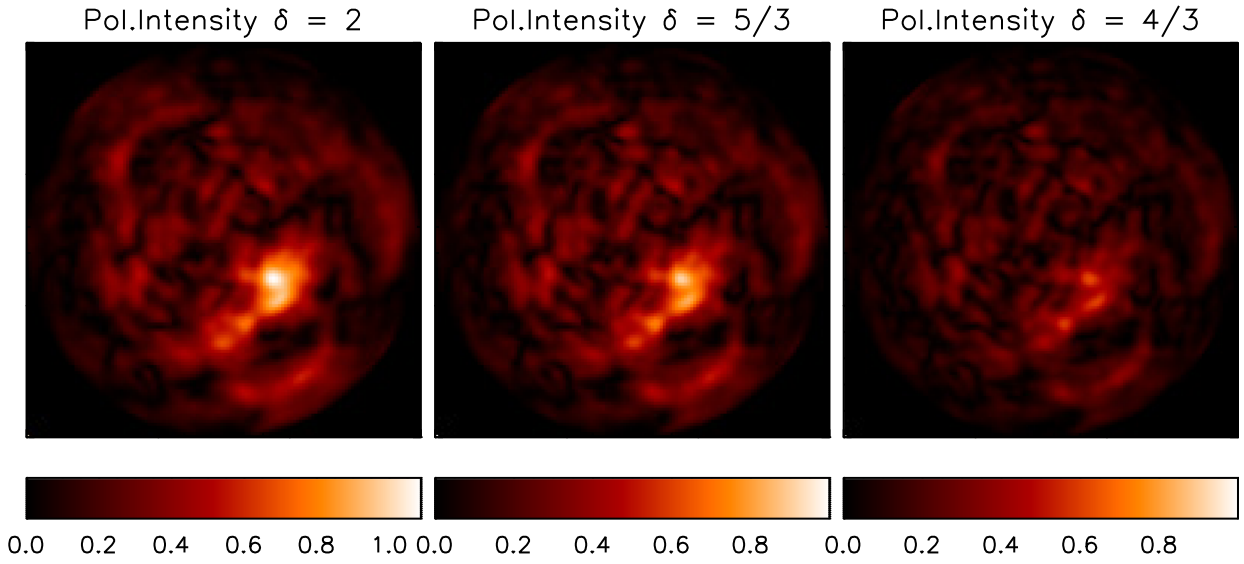


**Figure 1.** Polarized surface brightness maps, normalized to the mean total surface brightens, for the same magnetic realization (same orientations of the modes), but with various turbulent indexes, in the case of maximal helicity. The spectral index is set to $\alpha = 1/4$.

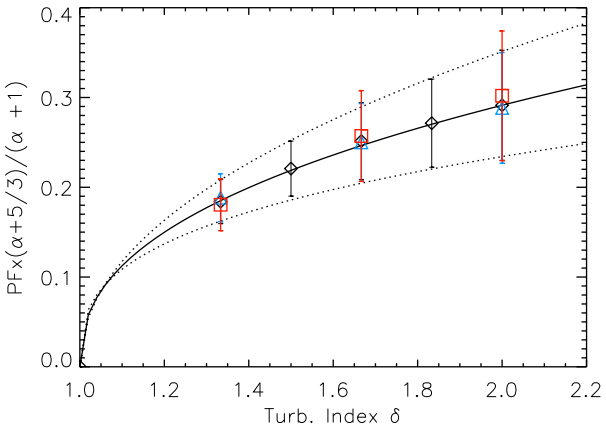


**Figure 2.** Integrated polarized fraction, *PF* normalized to the synchrotron factor $(\alpha + 1)/(\alpha + 5/3)$, as a function of the power spectral index of the turbulence $\delta$. Black diamonds are the mean values for $\alpha = 1/4$, blue triangles for $\alpha = 0$, and red squares for $\alpha = 1/2$. The error-bars represent the $2\sigma$ range.

dominated by the small scale components which carry most of the magnetic energy, hence the polarized fraction, which is instead due to the large scale components, vanishes.

We see immediately that the integrated polarized fraction shows a clear power-law dependence on the turbulent index, while the dependence on the distribution functions of the emitting pairs is, within the statistical uncertainty of our realizations, simply given by the standard synchrotron factor $(\alpha + 1)/(\alpha + 5/3)$. Indeed one can model our result with the simple relation:

$$\mathrm{Mean}[PF(\delta,\alpha)] = \frac{\alpha+1}{\alpha+5/3}[0.291(\delta-1)^{0.413}] \tag{24}$$

with the $2\sigma$ limits given by

$$[PF(\delta,\alpha)]^{+2\sigma} = \frac{\alpha+1}{\alpha+5/3}[0.351(\delta-1)^{0.476}] \tag{25}$$

$$[PF(\delta,\alpha)]_{-2\sigma} = \frac{\alpha+1}{\alpha+5/3}[0.234(\delta-1)^{0.333}]. \tag{26}$$

Obviously these fits apply only to the range of $\delta$ we have investigated. In particular, extrapolation to $\delta \to \infty$ would lead to $PF \to \infty$, which is unphysical. Indeed we find that, if only the mode $k = k_{11}$ is present, then the mean *PF* normalized to the spectral index factor is ∼0.45.

### 4.2 Zero helicity

At the other extreme with respect to the maximal helicity case, there are the zero helicity realizations with $c_{+nlm} = c_{-nlm}$. Attempts to define observables able to constrain the level of the helicity of the magnetic field, have been developed in the past, making use of higher order statistics and rotation measure (Waelkens et al. 2009; Junklewitz & Enßlin 2011). Here we focus on a simple estimate of the possible role of helicity over integrated quantities. It can easily be shown that for a magnetic field described as a simple linearly polarized plane wave the ratio of the polarized intensity over the total intensity is a constant for every direction of the observer, and in every position of the emitting domain, and the direction of polarization is also constant. For a magnetic field described as a circularly polarized plane wave, there are depolarization effects along the line of sight (the direction of $\boldsymbol{B} \wedge \boldsymbol{n}$ changes throughout the emitting domain). So it is reasonable to expect that a magnetic realization, with zero helicity, should show larger polarized fractions. How large would depend on the power spectrum of the turbulent realization. If the polarization properties of the simulated bubble are dominated by magnetic fluctuations of the largest scale to which only few modes of small $k$ contribute, then the dependence on the helicity will be pronounced. If on the other hand polarization is dominated by magnetic fluctuations on smaller scales, where many high $k$ modes contribute incoherently, then one would expect to see only small differences.

Given the power spectrum we have adopted for our magnetic field realizations, we found that the polarized fraction, *PF*, is almost completely set by the first few (∼5) modes at small $k$, for all the values of $\delta$ we have simulated. As a result the effects of a different helicity prescription are substantial. On Fig. 3 we show the same result of Fig. 2, but for $H = 0$. Note that again we find that the integrated polarized fraction can be described as a power-law

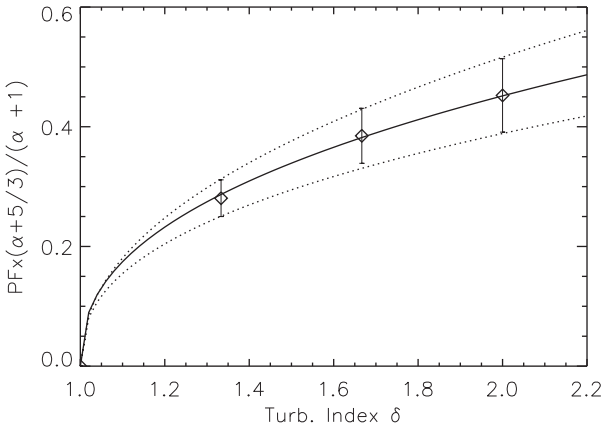


**Figure 3.** Integrated polarized fraction, *PF*, normalized to the synchrotron factor $(\alpha + 1)/(\alpha + 5/3)$, as a function of the power spectral index of the turbulence $\delta$, for the zero helicity case: $H = 0$. The spectral index is $\alpha = 1/4$. The solid curve is a power-law fit to the averages, and is just given by equation (24) multiplied by a factor of 1.52. The dotted curves represent power-law fit to the $2\sigma$ range.

function of the turbulent index, but the typical values are 50 per cent higher than the previous case and well beyond the $2\sigma$ range of variance. Even the variance of the distribution is now ∼50 per cent larger. Despite the fact that the case $\delta = 4/3$ has a flatter spectrum of magnetic turbulence than the $\delta = 2$ case, we do not see any appreciable, difference associated with the choice of helicity. This suggests that, even at $\delta = 4/3$, the large scales are still dominant.

### 4.3 Equipartition

The magnetic field given by equation (5) as the sum of force-free modes is itself not force free and as such it is out of dynamical equilibrium. In many situations of interest, like wind bubbles, to which our approach is targeted, the energy of the magnetic field is comparable to the one in the emitting plasma. It is common in these systems to assume equipartition between the particles and the field, in order to infer physical informations from the emission properties (Pacholczyk 1970). The validity of such an assumption is often confirmed by more sophisticated models of the spectral energy distribution. This requires the distribution of emitting particles to be highly correlated to the magnetic field. In general however, when dealing with possible variations of the density of emitting particles, it is customary to assume a complete uncorrelation. In order to model a distribution of emitting particles that follows an equipartition recipe, we modified equation (14) using a variable $K$ such that

$$K(\boldsymbol{r}) \propto (B^2_{\rm max} - B^2(\boldsymbol{r})), \tag{27}$$

where $B(\boldsymbol{r})$ is the magnetic field strength at position $\boldsymbol{r}$ and $B^2_{\rm max}$ is the maximum strength of the magnetic field in the unitary ball $\mathcal{B}$ (which differs in each realization). This ensures that the sum of the magnetic and particle energy is constant throughout the emitting volume.

Interestingly we find that the mean polarized fraction and its variance are unchanged with respect to the case of a uniform electron distribution, even if the surface brightness in the emission maps, appears shallower. Given that emission scales linearly with the particle number density, one can safely conclude that for an electron distribution given as

$$K(\boldsymbol{r}) = K_o + C(B^2_{\rm max} - B^2(\boldsymbol{r})), \tag{28}$$

the polarized fraction is independent of the value of $C$.

### 4.4 Cascade quenching and instrumental resolution

The results discussed previously assume that the turbulent cascade extends all the way to $k \to \infty$ and that maps have infinite spatial resolution. We can however take into account both the effect of turbulent quenching (if the cascade is truncated at a given $k_{\rm max}$) and of instrumental resolution. In Fig. 4 we show how the map of polarized intensity changes depending where the cascade is truncated. In Fig. 5 we plot the total intensity and polarized intensity, for some of our realizations, showing how they change depending on the truncation of the power-law distribution of the magnetic field. In particular the cutoff is parametrized in terms of the *relative cascade energy*: $1 - \delta E(k_{\rm max})/E(\infty)$.

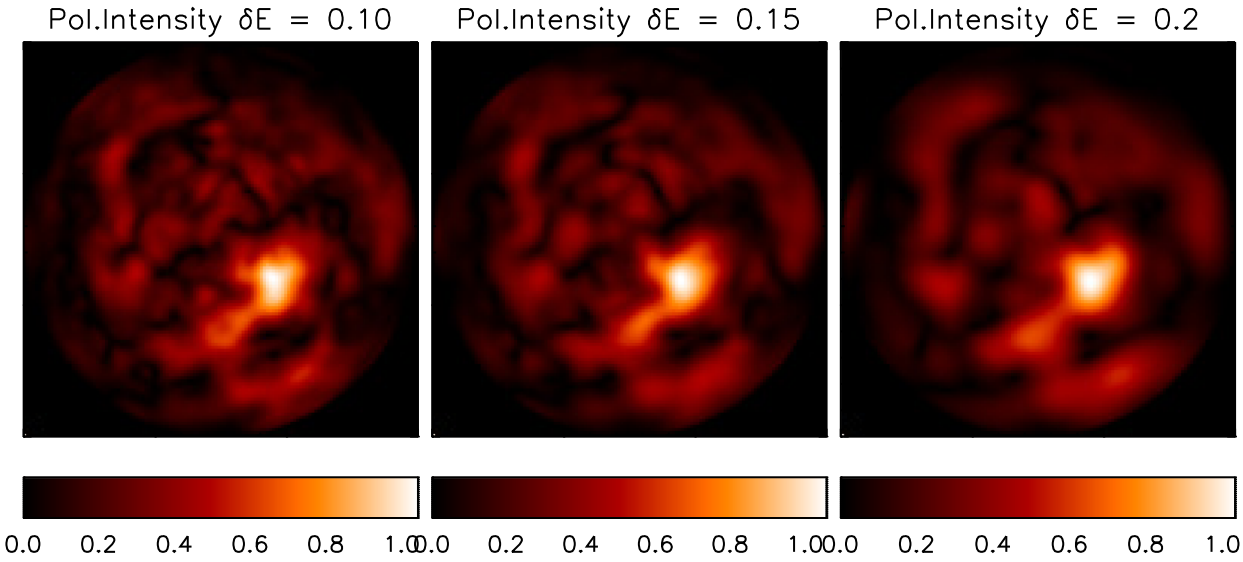


**Figure 4.** Polarized surface brightness maps, normalized to the mean total surface brightness, for the same magnetic realization (with $\delta = 2$ and $\alpha = 1/4$) in the case of maximal helicity, but for turbulent magnetic cascades truncated at various valued of $\delta E(k_{\rm max})$.

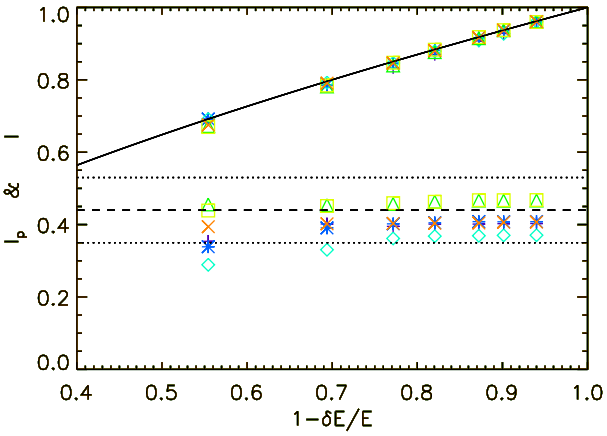


**Figure 5.** Trend of the total intensity and polarized intensity, as a function of cascade quenching, for the maximal helicity case $\delta = 2$ and $\alpha = 1/4$. The upper points correspond to the total intensity $I$ of several realizations as a function of $\delta E(k_{\rm max})/E(\infty)$ (each point-style/colour selects a realization set with a given configuration of the modes, progressively truncated at higher $k$). The lower points refer to the corresponding polarized intensity $I_{\rm p}$. $I$ and $I_{\rm p}$ are normalized to the total intensity in the limit $k \to \infty$. The solid line represents the function $[1 - (1 - \delta E(k_{\rm max}))^{(\alpha+1)/2})]$, that provides a good fit to the trend of the intensity. The dashed line represents the mean polarized fraction as given by equation (24) and the dotted lines the $2\sigma$ range as given by equations (26)–(25) for the limit $k_{\rm max} \to \infty$.

We find that in general the polarized intensity saturates already for values of $\delta E(k_{\rm max}) \sim 0.3E(\infty)$, coherently with our estimate in equation (23), on the other hand the total intensity keeps increasing quasi-linearly according to equation (22). This, as discussed, reflects the fact that while the total intensity is always a positively defined quantity, and so it increases with the addition of small scale modes, the polarized intensity is derived from Stokes parameters $U$ and $Q$, which are not positively defined, and so undergo cancellation effects. Interestingly we find that for $E(k_{\rm max}) > 0.6$ the following relation for the polarized fraction holds with a few per cent accuracy:

$$PF(E(k_{\rm max})) = [1 - (1 - \delta E(k_{\rm max}))^{(\alpha+1)/2})]^{-1} PF(E(\infty)), \quad (29)$$

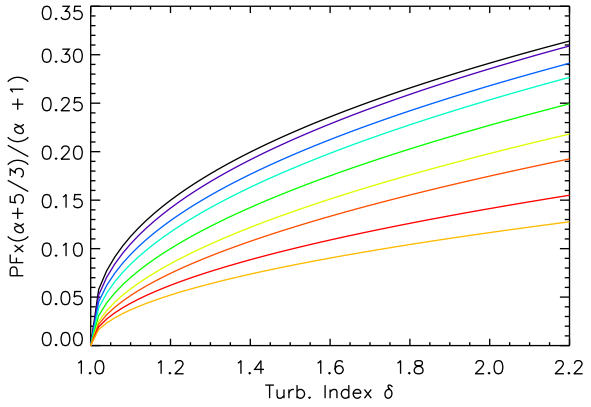


**Figure 7.** Best fits of the mean of the integrated polarized fraction, $PF$, normalized to the synchrotron factor $(\alpha + 1)/(\alpha + 5/3)$, as a function of the power spectral index of the turbulence $\delta$. The spectral index is $\alpha = 1/4$. The curves refer to different instrumental resolution. From top to bottom the FWHM of the point spread function is [0, 0.02, 0.04, 0.06, 0.10, 0.15, 0.20, 0.30, 0.40] times the diameter of the emitting bubble.

where $PF(E(\infty))$ corresponds to the polarized fraction of a cascade extending to $k = \infty$ and whose mean and variance are given in equations (24)–(26).

On the other hand, instrumental resolution acts to decrease the level of polarization because while not altering the total intensity, it introduces cancellation effects of the Stoke's parameters $U$ and $Q$. In Fig. 6 we show how the polarized emission maps change due to instrumental resolution assuming a Gaussian point spread function of varying width. Interestingly by comparing the first panel in Fig. 6 with the last one in Fig. 4, we see that on the morphology of the polarized emission, the effect of a truncated magnetic cascade is analogous to the one due to instrumental resolution. The two maps are hardly distinguishable, especially with reference to the brightest parts. What really distinguishes the two cases is the net polarized fraction because quenching and instrumental resolution, act differently on the total intensity. In Fig. 7, we show how the mean polarized fraction of our realizations changes, depending on instrumental resolution and for different values of $\delta$. Interestingly we find that even in this case, we can fit the dependence of the mean

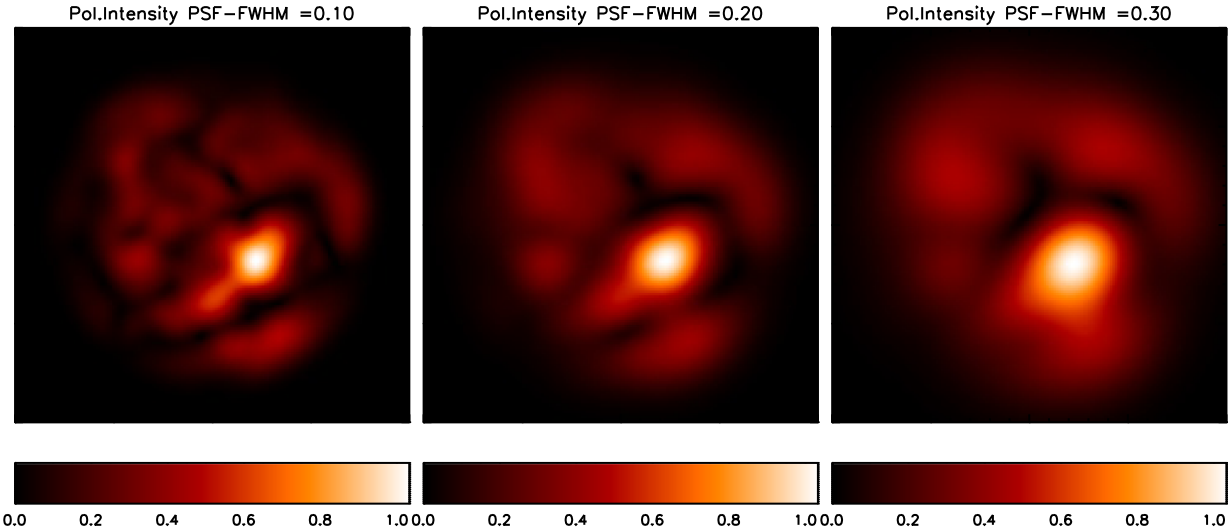


**Figure 6.** Polarized surface brightness maps, normalized to the mean total surface brightens, for the same magnetic realization (with $\delta = 2$ and $\alpha = 1/4$) in the case of maximal helicity, but for different FWHM of the point spread function. From left to right: 0.10, 0.20 and 0.30 times the diameter of the bubble.

value on $\delta$ with a power law. The variance instead shows only minor changes (at most ∼20 per cent) with respect to the case of infinite resolution.

By comparing Fig. 1 with Fig. 6 or Fig. 4, we see that the structure of the polarized emission changes. While for an infinite cascade, at a very high resolution, the polarized intensity, show many small scale features, in the other cases, these do not smear out into a more uniform map, but end up merging into larger structures that have the general shape of loops. Interestingly a similar pattern was seen in the body of G327.1-1.1 (Ma et al. 2016). It was also observed that the magnetic field direction seems to follow the loops. In that paper a model was put forward to explain the level of polarization and the typical scales observed, however due to the simplicity of the approach it was not possible to reproduce the loopy structure of the magnetic field and the correlation between direction and bright features. The authors suggested that a possible reason for this discrepancy was to be looked for in the fact that the model did not enforce the solenoidal condition on the magnetic field. In our model where the solenoidal condition is enforced by construction, we indeed recover exactly this kind of behaviour, with the direction of the magnetic field inferred from Stoke's parameter aligned with the bright features.

### 4.5 Two points correlation

In the previous sections we have investigated the trends of global integrated quantities, like the total polarized flux and fraction, which are easily accessible even to simple observations. Here, in order to provide a quantitative estimate of the small scale properties of our simulated maps, we investigate the two-points correlation function of the Stoke's parameters defined (in the case of $Q$ and analogously for $U$), as

$$Q_1 Q_2(\delta r_{12}) = Q(\boldsymbol{r}) Q(\boldsymbol{r} + \delta \boldsymbol{r}), \tag{30}$$

where 1 and 2 label the two points located respectively at $\boldsymbol{r}$ and $\boldsymbol{r} + \delta \boldsymbol{r}$, and $\delta r_{12} = |\delta \boldsymbol{r}|$. In the top panel of Fig. 8 we show, for a Komogorov distribution $\delta = 5/3$, the probability distribution $P$ of the value $Q_1 Q_2(\delta r_{12})$, normalized for convenience to the mean total surface brightness squared $\langle I \rangle^2$ as a function of the separation $\delta r_{12}$. It is evident the skewness of the distribution for $\delta r_{12} < 0.2R$, where the two point correlation function is dominated by positive values suggesting that the polarized features are correlated, while for $\delta r_{12} > 0.4R$, the distribution is symmetric pointing to uncorrelated features. This is made more evident in the bottom panel of Fig. 8, where the probability distribution is shown for various values of $\delta r_{12}$, and where the mean value of the two point correlation function is also shown.

## 5 CONCLUSIONS

In this work we have introduced a novel approach to the study of synchrotron emission from a turbulent magnetic field realization, based on a set of harmonic functions (the Chandrasekhar–Kendall functions) that allows us to take into account the geometrical properties of the source, and to enforce correct surface-boundary conditions, going beyond the standard small scale approximation, typical of many previous studies. This is particularly relevant for synchrotron emitting bubbles, where current instrumental resolution does not allow us to sample structures that are much smaller than the bubble size itself. The approach offers moreover the possibility to take into account anisotropy in the turbulent cascade and to control the level and distribution of helicity amongst the modes.

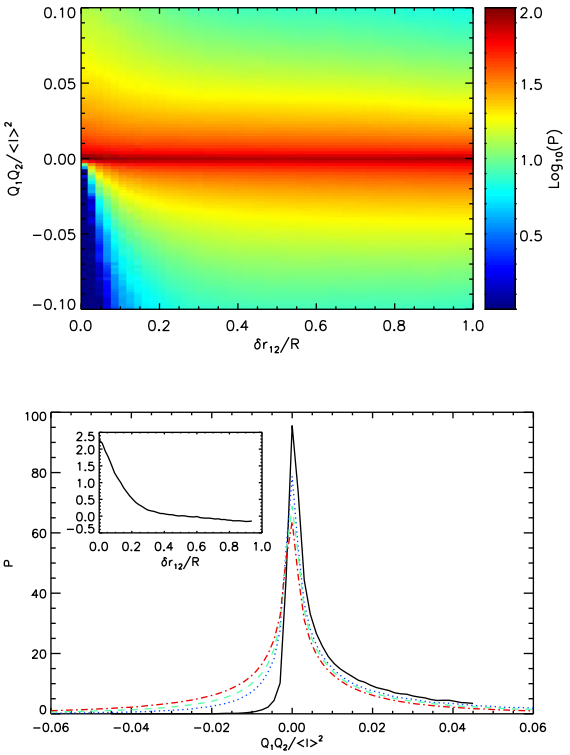


**Figure 8.** Upper panel: probability distribution function of the two-point correlation $Q_1 Q_2(\delta r_{12})$ normalized to the mean squared total surface brightness $\langle I \rangle^2$, as a function of the separation between the two points $\delta r_{12}$. Lower panel: probability distribution function of the two-point correlation $Q_1 Q_2(\delta r_{12})$ for selected values of $\delta r_{12}$: 0.02 solid-black line, 0.1 dotted-blue line, 0.2 dashed-green line, 0.5 dash-dotted-red line. The insert shows the average value of $Q_1 Q_2(\delta r_{12})/\langle I \rangle^2$ (multiplied times 100), as a function of $\delta r_{12}$.

We try to investigate how global properties, like the integrated polarized fraction, scale depending on the spectrum of turbulence, helicity distribution, spectral index of the emitted radiation, resolution and cascade quenching. Interestingly we found that the spatial distribution of the emitting particles (either uniform or anticorrelated with the magnetic field strength) does not affect such global properties. While the dependence on the spectral index (tied to the particle distribution function) follows the standard synchrotron law. We found that the mean polarized fraction of our realizations can be fitted with a power law with respect to the turbulent index $\delta$ and that this trend holds also for different helicity and instrumental resolution.

To illustrate an application of our results, let us consider for example G327.1-1.1 (Ma et al. 2016). This is a middle age pulsar wind nebula with the pulsar outside the main radio body of the nebula. In radio a loopy structure is observed, with the magnetic field inferred from linear polarization aligned with the bright features. The spectral index in radio is $\alpha = 0.3$. The body observed at 3 cm and 6 cm, with a resolution corresponding to a full-width half-maximum (FWHM) ∼0.05 times the nebular diameter, shows an average polarized fraction $\sim 15 - 20$ per cent, with a single highly polarized spot ∼30 per cent at the centre, and an increasing polarization towards the edges, mostly an artefact due to the low local surface brightness. With reference to Fig. 7 we find that the lower value coincides with the expected mean of PF in the Kolmogorov case $\delta = 5/3$, with maximal helicity, while the upper limit, higher than the $2\sigma$ range, would suggest some cascade quenching with

$\delta E \sim 0.7E(\infty)$. Obviously, taking into account the typical variance of our realizations, the detected polarized fraction, is compatible with turbulent spectra in the range $1.5 < \delta < 2.1$, and the upper limit could be due to a different helicity. It is however interesting that our model allows us, to set some constraint on the turbulence inside such system: the preferred model suggests a Kolmogorov turbulence, either with low helicity or some quenching.

## ACKNOWLEDGEMENTS

The author acknowledges support from the PRIN–MIUR project prot. 2015L5EE2Y, *Multi-scale simulations of high-energy astrophysical plasmas*.

## REFERENCES

Baade W., 1956, Bull. Astron. Inst. Neth., 12, 312
Begelman M. C., Cioffi D. F., 1989, ApJ, 345, L21
Begelman M. C., Blandford R. D., Rees M. J., 1984, Rev. Mod. Phys., 56, 255
Blondin J. M., Chevalier R. A., Frierson D. M., 2001, ApJ, 563, 806
Brandenburg A., 2011, Pramana, 77, 67
Brandenburg A., Lazarian A., 2013, Space Sci. Rev., 178, 163
Bucciantini N., 2008, in Bassa C., Wang Z., Cumming A., Kaspi V. M., eds, Am. Inst. Phys. Conf. Ser. Vol. 983, 40 Years of Pulsars: Millisecond Pulsars, Magnetars and More. Am. Inst. Phys., New York, p. 186
Bucciantini N., Amato E., Bandiera R., Blondin J. M., Del Zanna L., 2004, A&A, 423, 253
Bucciantini N., Bandiera R., Olmi B., Del Zanna L., 2017, MNRAS, 470, 4066
Burlaga L. F., 1988, J. Geophys. Res., 93, 7217
Carilli C. L., Perley R. A., Harris D. E., 1994, MNRAS, 270, 173
Chandra S., 1987, Ap&SS, 136, 409
Chandra S., Prasad L., 1991, Sol. Phys., 134, 99
Chandrasekhar S., Kendall P. C., 1957, ApJ, 126, 457
Dasgupta B., Janaki M. S., Bhattacharyya R., Dasgupta P., Watanabe T., Sato T., 2002, Phys. Rev. E, 65, 046405
Deredtsov E. Y., Kasantsev S. G., Schuster T., 2007, J. Inv. Ill-Posed Probl., 15, 19
Farrugia C. J., Osherovich V. A., Burlaga L. F., 1995, J. Geophys. Res., 100, 12
Frail D. A., Giacani E. B., Goss W. M., Dubner G., 1996, ApJ, 464, L165
Gaensler B. M., Slane P. O., 2006, ARA&A, 44, 17
Giacani E. B., Dubner G. M., Kassim N. E., Frail D. A., Goss W. M., Winkler P. F., Williams B. F., 1997, AJ, 113, 1379
Goldreich P., Sridhar S., 1995, ApJ, 438, 763
Herron C. A., Burkhart B., Lazarian A., Gaensler B. M., McClure-Griffiths N. M., 2016, ApJ, 822, 13
Ivanov K. G., Kharshiladze A. F., 1985, Sol. Phys., 98, 379
Junklewitz H., Enßlin T. A., 2011, A&A, 530, A88
Jun B.-I., 1998, ApJ, 499, 282
Kennel C. F., Coroniti F. V., 1984, ApJ, 283, 710
Lazarian A., Pogosyan D., 2012a, ApJ, 747, 5
Lazarian A., Pogosyan D., 2012b, ApJ, 747, 5
Lazarian A., Pogosyan D., 2016, ApJ, 818, 178
Lazaryan A. L., Chibisov G. V., 1991, Sov. Astron. Lett., 17, 208
Lazaryan A. L., Shutenkov V. P., 1990, Soviet Astronomy Lett., 16, 297
Legg M. P. C., Westfold K. C., 1968, ApJ, 154, 499
Liao Z.-J., Su W.-D., 2015, Phys. Fluids, 27, 041701
Ma Y. K., Ng C.-Y., Bucciantini N., Slane P. O., Gaensler B. M., Temim T., 2016, ApJ, 820, 100
Marsh G. E., 1992, Phys. Rev. A, 45, 7520
Mininni P. D., Montgomery D. C., 2006, Phys. Fluids, 18, 116602
Mininni P. D., Montgomery D. C., Turner L., 2007, New J. Phys., 9, 303
Molodensky M. M., 1974, Sol. Phys., 39, 393
Morse E. C., 2005, J. Math. Phys., 46, 113511
Morse E. C., 2007, J. Math. Phys., 48, 083504
Olmi B., Del Zanna L., Amato E., Bucciantini N., 2015, MNRAS, 449, 3149
Olmi B., Del Zanna L., Amato E., Bucciantini N., Mignone A., 2016, J. Plasma Phys., 82, 635820601
Oort J. H., Walraven T., 1956, Bull. Astron. Inst. Neth., 12, 285
Pacholczyk A. G., 1970, Radio Astrophysics. Nonthermal Processes in Galactic and Extragalactic Sources, Freeman & Co., San Francisco
Pacini F., Salvati M., 1973, ApJ, 186, 249
Porth O., Komissarov S. S., Keppens R., 2014, MNRAS, 443, 547
Rasband S. N., Turner L., 1981, Phys. Fluids, 24, 931
Rees M. J., Gunn J. E., 1974, MNRAS, 167, 1
Reich P., Testori J. C., Reich W., 2001, A&A, 376, 861
Roberts M. S. E., Romani R. W., Johnston S., Green A. J., 1999, ApJ, 515, 712
Scheuer P. A. G., 1982, in Heeschen D. S., Wade C. M., eds, IAU Symp. 97, Extragalactic Radio Sources. Kluwer, Dordrecht, p. 163
Tanaka S., Asano K., 2016, in Supernova Remnants: An Odyssey in Space after Stellar Death, p. 57
Tang X., Chevalier R. A., 2012, ApJ, 752, 83
Thiébaut J., Prunet S., Pichon C., Thiébaut E., 2010, MNRAS, 403, 415
Vandas M., Fischer S., Geranios A., 1991, Planet. Space Sci., 39, 1147
Vandas M., Fischer S., Odstrčil D., Dryer M., Smith Z., Detman T., 1997, in Crooker N., Joselyn J. A., Feynman J., eds, Geophys. Monogr. Ser. Vol. 99, Coronal Mass Ejections. Am. Geophys. Union, Washington DC, p. 169
Waelkens A. H., Schekochihin A. A., Enßlin T. A., 2009, MNRAS, 398, 1970
Westfold K. C., 1959, ApJ, 130, 241
Woltjer L., 1958a, Bull. Astron. Inst. Neth., 14, 39
Woltjer L., 1958b, ApJ, 128, 384
Yoshida Z., 1992, J. Math. Phys., 33, 1252
Zhang J.-F., Lazarian A., Lee H., Cho J., 2016, ApJ, 825, 154

This paper has been typeset from a TEX/LATEX file prepared by the author.